Structure of fibrin gels studied by elastic light scattering techniques: Dependence of fractal dimension, gel crossover length, fiber diameter, and fiber density on monomer concentration

Fabio Ferri,[1,*] Maria Greco,[1] Giuseppe Arcòvito,[2] Marco De Spirito,[2] and Mattia Rocco[3]
[1]*Dipartimento di Scienze Chimiche, Fisiche e Matematiche and INFM, Università dell'Insubria a Como, via Valleggio 11, I-22100 Como, Italy*
[2]*Istituto di Fisica, Facoltà di Medicina e Chirurgia and INFM, Università Cattolica del Sacro Cuore, Largo F. Vito 1, 00168 Roma, Italy*
[3]*U. O. Biologia Strutturale, Istituto Nazionale per la Ricerca sul Cancro (IST), c/o Centro Biotecnologie Avanzate (CBA), Largo R. Benzi 10, 16132 Genova, Italy*
(Received 14 January 2002; published 26 July 2002)

The concentration dependence of the structure of fibrin gels, formed following fibrinogen activation by thrombin at a constant molar ratio, was investigated by means of elastic light scattering techniques. The scattered intensity distributions were measured in absolute units over a wave-vector range q of about three decades ($\sim 3\times10^{2}-3\times10^{5}$ cm^{-1}). A set of gel-characterizing parameters were recovered by accurately fitting the data with a single function recently developed by us [F. Ferri *et al.*, Phys. Rev. E **63**, 031401 (2001)], based on a simple structural model. Accordingly, the gels can be described as random networks of fibers of average diameter d and density ρ, entangled together to form densely packed and spatially correlated blobs of mass fractal dimension D_m and average size (or crossover length) ξ. As previously done for d, we show here that the recovered ξ is also a good approximation of a weight average, namely, $d\sim\sqrt{\langle d^2\rangle_w}$ and $\xi\sim\langle\xi\rangle_w$. By varying the fibrinogen concentration c_F between 0.034–0.81 mg/ml, gels with $100\geqslant\xi\geqslant10$ μm, $100\leqslant d\leqslant200$ nm, $1.2\leqslant D_m\leqslant1.4$, and constant $\rho\sim0.4$ mg/ml were obtained. The power-law c_F dependencies that we found for both ξ and d are consistent with the model, provided that the blobs are allowed to partially overlap by a factor η likewise scaling with c_F ($2\geqslant\eta\geqslant1$). Recasting the whole dataset on a single master curve provided further evidence of the similarity between the structures of all the gels, and confirmed the self-consistency of the model.

DOI: 10.1103/PhysRevE.66.011913 PACS number(s): 87.15.−v, 82.35.−x, 82.70.−y

I. INTRODUCTION

Fibrin gels are the main structural scaffolds of the hemostatic plug formed in vertebrate blood coagulation [1,2]. They also play important roles in various physiological and pathological situations, including cancer [3], and they have attracted much attention for their biotechnological potential (see Ref. [4] and references therein). Fibrin gels are grown from the polymerization of fibrinogen, a high molecular weight centrosymmetric macromolecule (molecular weight $=340\,000$), rodlike in shape, $\sim$50 nm long, $\sim$5 nm thick, composed of two pairs each of three different chains, covalently linked at their *N*-termini [1,2,5]. Basically, the molecule consists of a central globular domain joined by two elongated connectors to two identical outer domains. The central domain contains two pairs of knoblike bonding sites *A* and *B*, while a pair of the complementary polymerization ''holes'' *a* and *b* is located in each of the outer domains. The *A* and *B* sites are masked by short peptides, which can be enzymatically removed leading to the formation of a rapidly polymerizing species called fibrin monomer [1,2]. As a result of the *Aa* interactions, half-staggered, double-stranded, wormlike fibrils are initially produced [1,2,6,7]. Then, enhanced also by the formation of the *Bb* bonds, the fibrils aggregate laterally and start to branch, eventually giving rise to a gel [1,2,6].

Fibrin gels have been intensively studied for many decades, with important contributions coming from electron microscopy and light scattering techniques (see Refs. [1,2,7], and references therein). These studies have shown that fibrin gels are three-dimensional networks made of entangled fibers whose physical properties (average size, spatial distribution, extent of branching, flexibility, and so on) determine the properties of the entire network, such as its morphology, porosity, and elasticity. By varying the physical-chemical conditions of the gelling solution, such as the pH, the presence of ions of different type and concentration, and the activating enzyme, one can obtain gels with very different characteristics (see Ref. [8] and references therein). There are two limiting classes in which fibrin gels are customarily classified: ''coarse,'' large-pore gels made of thick fibers, and ''fine,'' narrow-pore gels made of thin fibers.

The aim of this paper is to extend the light scattering study [9] that we have recently carried out on some coarse fibrin gels formed from the polymerization of fibrinogen monomers under quasiphysiological conditions, with the reaction being initiated by monomer activation via the enzyme thrombin. In that work [9], the scattered intensity distributions were measured in absolute units and were taken both while the solution was gelling, and after the formation of a gel with a steady-state structure. By combining the low-angle elastic light scattering (LAELS) and the classical light scattering (CLS) techniques, an overall wave-vector range of about three decades, from $q\sim3\times10^{2}$ to $q\sim3\times10^{5}$ cm^{-1}, was covered. The main features of these distributions were

*Author to whom correspondence should be addressed. Dipartimento di Scienze Chimiche, Fisiche e Matematiche, Università dell'Insubria a Como, via Valleggio 11, I-22100 Como, Italy; FAX: +39-031 238-6209; E-mail address: fabio.ferri@uninsubria.it

the very low intensity scattered in the limit of zero angle, the presence of a peak at low q values, and the presence of a sharp rolloff at high q values, beyond which the intensity decays very rapidly. The data were interpreted in terms of a simple structural model, which describes the gel as an assembly of densely packed fractal blobs of average size ξ and mass fractal dimension D_m. Each blob is made of entangled fibers characterized by an average diameter d, density ρ, and surface fractal dimension D_s. Based on this model, a single fitting function able to reproduce the behavior of the intensity distribution over the whole wave-vector range was devised, and all the above parameters were recovered.

In this work, we investigate how the parameters characterizing the gel structure (i.e., d, ρ, ξ, and D_m) depend on the fibrinogen concentration c_F at a fixed molar ratio with the activating enzyme. We prepared a variety of gels under the same physical-chemical conditions of the gelling solution, with c_F varying over more than a decade, between 0.034–0.81 mg/ml. To account for the c_F dependence of the measured parameters, the model proposed in Ref. [9] was further developed with the introduction of one more parameter, η, which describes the linear filling ratio, or overlapping, between the blobs. The effects of polydispersity on the recovered parameters were also analyzed in more detail. The overall self-consistency of the model was finally verified by using scaling concepts and recasting all the data relative to the different concentrations on a single master curve.

II. EXPERIMENTAL

Human fibrinogen and thrombin were purchased from Calbiochem, San Diego, CA, USA (Cat. No. 341576, lot B10707) and Sigma-Aldrich, Milano, Italy (Cat. No. I-6759, lot 104H9314, ~2000 NIH units/mg protein), respectively. Tris-hydroxymethyl-aminomethane free base (Tris) and the hydrochloride form (Tris-HCl) and all other chemicals were of reagent-grade from Merck (Bracco, Milano, Italia). Double-distilled water was always used throughout this study. The polymerizations were carried out in a Tris 50 mM, NaCl 0.1 M, EDTA-Na_2 (EDTA, ethylenediamine tetraacetic acid) 1 mM, pH 7.4 (TBE) buffer. For each concentration, the activation rate of the monomers was maintained the same by fixing the molar ratio between the activating enzyme (thrombin) and fibrinogen to 1:100. Under these conditions, the initial polymerization process is limited by the rate of activation of the monomers that react and polymerize (see Ref. [7] and references therein). The effective enzyme concentration (i.e., the concentration of the enzyme active site) was determined by the method of Dang and Di Cera [10]. Accordingly, thrombin was diluted to ~1 nM with a 100 mM NaCl, 5 mM Tris, pH 8.0 buffer solution. Hirudin (Ciba-Geigy Pharmaceuticals, Horsham, England), a practically irreversible thrombin inhibitor, was added to the solution at concentrations ranging from 0 to 1 nM. Then the chromogenic substrate H-D-Phe-Pip-Arg-pNA (S-2238, Chromogenix, Milano, Italy) was added to each solution at 20 mM final concentration, and the reaction was followed spectrophotometrically at $\lambda = 405$ nm. The effective enzyme concentration was finally determined from the slope and the intercept of a plot of the initial reaction velocity vs inhibitor concentration [10]. An evaluation of the thrombin activity in NIH units was later carried out by comparing the clotting times with those obtained with a newer batch. Fibrinogen purification by size-exclusion chromatography, samples preparation, and controls, were all carried out as previously reported [9,11].

A detailed description of the two experimental light scattering setups used in this study has also been already presented [9]. Here, it will suffice to say that the homemade LAELS apparatus used a 5 mW He-Ne laser light source to illuminate the samples placed in thermostatted ($25 \pm 0.1\,^{\circ}$C) 2 or 5 cm thick quartz cuvettes. The scattered light was collected simultaneously at up to 30 scattering angles θ corresponding to a practical wave-vector range from $q \sim 3 \times 10^2$ to $q \sim 3 \times 10^4$ cm^{-1}, with $q = 4\pi n/\lambda_0 \sin(\theta/2)$, $\lambda_0 = 632.8$ nm being the incident wavelength *in vacuo* and n the refractive index of the medium (1.3340 at 632.8 nm for TBE, see Ref. [7]). The CLS instrument was a commercial ALV/SLS-5000 system (ALV, Langen, FRG) powered by a 4 W argon laser (Innova 70, Coherent, FRG) operating at $\lambda_0 = 488$ nm ($n = 1.3392$ for TBE) and delivering ~100–200 mW on the sample, contained in 0.8 cm inner diameter quartz cylindrical cuvettes held at $25 \pm 0.1\,^{\circ}$C in a thermostatted index-matching vat. The scattered light was collected at several angles, covering a q range of $\sim 4 \times 10^4 - 3 \times 10^5$ cm^{-1}, by a monomode fiber coupled to a photomultiplier, both mounted on a rotating arm. In addition, the scattering cell was simultaneously rotated and translated along the vertical axis during the measurements to average the scattered intensity over many different spatial configurations [9].

III. DATA ANALYSIS AND MODELING

In this section, we will first recall the main features of the model proposed recently [9] to describe the structure of an aged gel, and then we will implement such a model for the analysis of the scattering data taken on gels prepared at different monomer concentrations.

As sketched in Fig. 1, the aged gel can be imagined as a collection of spatially correlated fractal blobs of size ξ and mass fractal dimension D_m. The parameter ξ was also called crossover length of the gel [9]. Since the blobs are densely packed, their size is comparable with their average distance ξ_0, i.e., $\xi \sim \xi_0$. Each blob is made of an assembly of n segments or ''building blocks'' that can be sketched as cylindrical objects with diameter d and length ℓ. Thus, $n \sim (\xi/\ell)^{D_m}$, and the blob molecular weight M is given by

$$M \sim N_A \frac{\rho \pi}{4} \ell^{1-D_m} \xi^{D_m} d^2, \tag{1}$$

where ρ is the segment density and N_A is the Avogadro number.

The intensity distribution $R(q)$ scattered by such a system can be written as the product of two terms: a structure factor $S(q)$ that describes the spatial correlation between each blob's center of mass, and a form factor $P(q)$ that describes the internal structure of each blob,

$$R(q)=K\,c_F\,M\,\underbrace{[1-\beta e^{-(\gamma\xi q)^2}]}_{S(q)}\underbrace{\left[\frac{1}{[1+(q\xi/\pi)^2]^{D_m/2}}+\left(\frac{\ell}{\xi}\right)^{D_m}\right]}_{A(q)}\underbrace{\frac{1}{\left(1+q^2d^2\sqrt{\frac{\ell}{32d}}\right)^{\alpha_s/2}}}_{B(q)} \tag{2}$$

where the product $P(q)=A(q)B(q)$ is the "particle" form factor, c_F the fibrinogen concentration, and K is the usual optical constant [9,12]. The dimensionless parameters β and γ represent the amplitude and the range of spatial correlation among blobs, respectively, while α_s describes the surface properties of the fibers and is related to their surface fractal dimensions by $D_s=6-\alpha_s$. It should be stressed that Eq. (2) has been developed for a monodisperse system, i.e., a gel in which all the blobs have the same size ξ and same fiber diameter d. Some of the effects of polydispersity on the recovered parameters have been already addressed in our previous work [9], and will be further discussed in Appendix A.

Equation (2) is the function we will use for fitting our scattering data. In order to illustrate its main features, we report in Fig. 2 the behavior of $R(q)$ against q (open symbols) obtained by setting $c_F=0.1$ mg/ml, $\rho=0.4$ g/cm^3, $\xi=20\ \mu$m, $D_m=1.3$, $d=150$ nm, $\ell=0.4\ \mu$m, $\beta=1$, $\gamma=0.28$, and $\alpha_s=4$. The values assigned to the gel concentration c_F as well as to the parameters ρ, ξ, D_m, d, and ℓ correspond to those derived from one of our gels, while the remaining ones (β, γ, and α_s) were chosen according to physical considerations based on the model and will be discussed below. For a real comparison with the experimental conditions, the actual q intervals of the LAELS and CLS measurements are also reported.

The figure shows that there are three different regimes, delimited by the two wave vectors q_p and q_x. These three regimes are clearly determined by the three factors $S(q)$, $A(q)$, $B(q)$ of which $R(q)$ is the product, and are represented by the three solid straight lines in the figure. It should be noticed that $R(q)$ is reported in absolute units (cm^{-1}). Thus, the recovery of the parameter ρ from the fitting is a direct consequence of this fact, because ρ appears only in the amplitude prefactor of Eq. (2).

The behavior for $q \ll q_p$ is determined by the parameters β and γ. The parameter $\beta=1$ implies that $R(0)=0$, as expected for a system in which the blobs are densely packed [9]. Similarly, the value assigned to the parameter $\gamma=1/2\sqrt{\pi}\sim 0.28$ derives [9] from the assumption that $\xi=\xi_0$.

The peak indicates the presence of a long-range order in the structure of the gel, due to the spatial correlation between the blobs. The blob size (or gel crossover length) ξ is related to the peak position via the correspondence [9]

$$\xi\sim 1.3\pi^{2/(2+D_m)}\gamma^{-2/(2+D_m)}(q_p)^{-1}, \tag{3}$$

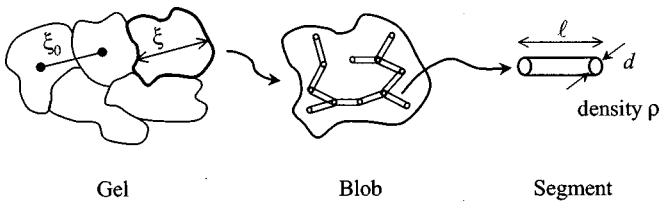

FIG. 1. Sketch of the gel structure based on the blob model described in the text: ξ is the blob size while ξ_0 is the average distance between blobs. The sketch is relative to a gel with no overlapping between the blobs, in which $\xi\sim\xi_0$. Each blob is a fractal assembly of segments of length ℓ, diameter d, and density ρ, joined together end-to-end with only a few branching points. The segment length ℓ should not be confused with the average fiber length between the branching points, but is rather likely related to the persistence length of the fibers [9].

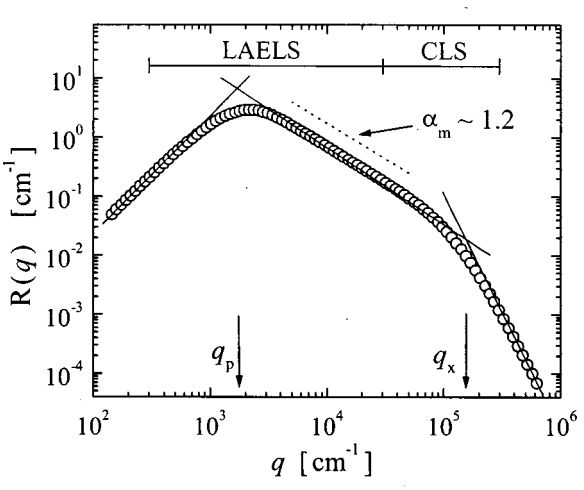

FIG. 2. Behavior of the fitting function $R(q)$ as a function of the wave vector q. The symbols refer to synthetic data generated according to Eq. (2) with $c_F=0.1$ mg/ml, $\rho=0.4$ g/cm^3, $\xi=20\ \mu$m, $D_m=1.3$, $d=150$ nm, $\ell=0.4\ \mu$m, $\beta=1$, $\gamma=0.28$, and $\alpha_s=4$. The solid straight lines show the three asymptotic regimes delimited by the two wave vectors q_p and q_x. The dotted line shows that the apparent power-law decay exponent is $\sim 1.2<D_m$. The LAELS and CLS intervals represent the actual wave-vector ranges probed in the measurements.

in which the numerical factor 1.3 takes into account the difference between the actual peak position and the value obtained as the intercept between the two leftmost solid straight lines of Fig. 2. For the specific case of Fig. 2 ($\gamma=0.28$, $D_m=1.3$), we have $q_p\xi\sim 4.4$. As mentioned above, Eq. (3) is valid for a monodisperse system. We will show in Appendix A that, when a gel made of blobs polydisperse in size and fiber diameter is considered, Eq. (3) is still valid, but with ξ replaced by an x-average size $\langle\xi\rangle_x$, which, even for very broad distributions, is a close approximation of the weight-average blob size $\langle\xi\rangle_w$. Thus, for a polydisperse gel, the peak position provides information on $\langle\xi\rangle_w$.

For $q_p \ll q \ll q_x$, the behavior of $R(q)$ is determined by the arrangement of the segments inside the blobs. If, within this range, the condition $\xi^{-1} \ll q \ll \ell^{-1}, d^{-1}$ is satisfied, we are in the fractal regime, where the mass fractal dimension D_m characterizes the power-law decay of $R(q)$. Indeed, in this region the spatial correlation among blobs are not important $[S(q)=1]$, the segments behave as point scatterers $[B(q)=1]$, and the blob form factor is $P(q)=(\pi/q\xi)^{D_m}$. Thus, Eq. (2) can be approximated to

$$R(q)=Kc_F M\left(\frac{q\xi}{\pi}\right)^{-D_m}, \tag{4}$$

which, by using Eq. (1) for M, becomes

$$R(q)=\frac{\pi^{1+D_m}}{4}Kc_F N_A \rho \ell^{1-D_m} d^2 q^{-D_m}. \tag{5}$$

Equation (5) shows that, in the fractal regime, the scattered intensity decays as a power law with an exponent equal to the fractal dimension D_m and with an amplitude that depends, besides c_F, on the parameters ρ, ℓ, and d, but not on ξ and γ. However, it should be pointed out that Eq. (5), which is graphically represented by the central solid straight line of Fig. 2, does not reproduce the behavior of the curve very accurately. Indeed, the data appear to follow a power-law decay, but with a somewhat smaller exponent $\alpha_m\sim 1.2$, as shown by the dotted segment reported in the figure. This is due to the fact that the condition that defines the right-hand side of the fractal regime ($q \ll \ell^{-1}, d^{-1}$) is not fulfilled with high accuracy over the entire wave vector range where the LAELS data appear to be straight. We will return to this point in Appendix B, and discuss it quantitatively. Finally, it is worth noticing that in the particular case when $D_m=1$, the dependence of Eq. (5) on ℓ disappears and the well known expression for the scattering from cylinders [12] (i.e., objects with $D_m=1$) is obtained.

For $q>q_x$, there is a crossover to a behavior typical of surface fractals in which $R(q)$ decays much faster, with a power-law behavior characterized by the exponent α_s. The value $\alpha_s=4$ corresponds to fibers with a surface completely smooth and characterized by a sharp interface with the solvent ($D_s=2$). The intercept of the two asymptotes that define the fractal and the surface regimes defines the crossover wave vector q_x and allows an estimate of the average fiber diameter d. The corresponding relation is

$$q_x d\sim 2.2, \tag{6}$$

which holds almost independently [9] of D_m and ℓ. We conclude this part by recalling that, as we showed before [9], when gels made of blobs polydisperse in size and fiber diameter are considered, the diameter d that appears in both Eqs. (5) and (6) is actually a root-mean-square weight-average diameter, i.e., $d\sim\sqrt{\langle d^2\rangle_w}$.

We will now implement the model based on the blobs close packing condition. Equation (3) shows that the parameters ξ and γ are strongly correlated and, therefore, it is difficult to recover both of them from the fitting. As a matter of fact, we fit the data by fixing γ and letting ξ vary. Thus, the value recovered for ξ depends on the value assigned to γ. In view of the analysis as a function of c_F reported below, the condition $\gamma=0.28$ (or equivalently $\xi=\xi_0$) equal for all the gels [9], appears to be rather restrictive. Thus we found it convenient to introduce one more parameter, η, which represents the level of (linear) filling ratio or overlapping between the blobs. The parameter η can be defined as

$$\xi=\eta\xi_0 \tag{7}$$

meaning that, if $\eta=1$ the blobs are closely packed and just ''touch'' each other, if $\eta<1$ they are ''close'' but not in contact, and if $\eta>1$ they overlap. This also implies that while for $\eta=1$ ξ can be taken as an upper bound to the mesh size of the gel [9], when $\eta\neq 1$ this does not hold anymore. We will return to this point in Sec. VII.

The parameters η and γ are related to each other. By following the same analysis carried out in Ref. [9] [see Eqs. (6) and (7) of Ref. [9]] and by using Eq. (7) above, it is straightforward to show that

$$\gamma=\frac{1}{2\sqrt{\pi}}\eta^{-1}. \tag{8}$$

Therefore, by inserting Eq. (8) into Eq. (3) we have

$$\xi\sim 1.3(4^{1/(2+D_m)}\pi^{(1+D_m)/(2+D_m)})\eta^{2/(2+D_m)}(q_p)^{-1}. \tag{9}$$

Clearly, for $\eta=1$, Eqs. (3) and (9) coincide.

In order to investigate how the parameter η depends on c_F, we can use the blob model and the close packing condition (with overlapping) to find an explicit relation between ξ and c_F. For the sake of simplicity, we will consider here a monodisperse system. Polydispersity effects are deferred to Appendix A. Since the average distance between the blobs is ξ_0, the volume available for each blob is $\sim\xi_0^3$, and, consequently, the sample concentration can be written as $c_F\sim(M/N_A)/\xi_0^3$. By using Eqs. (1) and (7), it is straightforward to show that ξ scales with c_F according to

$$\xi\sim c_F^{-1/(3-D_m)}\eta^{3/(3-D_m)}\left[\frac{\pi}{4}\rho\ell^{1-D_m}d^2\right]^{1/(3-D_m)}, \tag{10}$$

predicting that, if the dependence of ξ on c_F is the dominant one, denser gels are made of smaller blobs and their size scales as $\sim c_F^{-1/(3-D_m)}$. As a comparison with other studies,

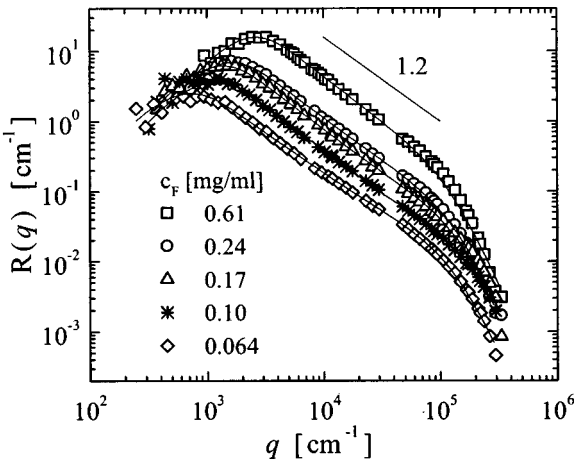

FIG. 3. Log-log plot of the scattered intensity distributions $R(q)$ as a function of the wave vector q for five fibrin gels prepared in a 0.1 M NaCl, 0.05 M Tris, 1 mM EDTA-Na_2, pH 7.4 (TBE) buffer solution, with the molar ratio thrombin:fibrinogen fixed to 0.01. The solid lines are the best fits of the data to Eq. (2).

it is interesting to notice that a relation similar to Eq. (10) was found to hold for different types of colloidal gels [13,14] and for some polymeric silica gels [15]. In those cases the building blocks of the blobs were ''spherical'' particles (for which $\ell = d$) with d equal for all the samples, regardless of c_F, and the overlapping parameter was $\eta = 1$.

In conclusion, we have two expressions describing the dependence of ξ on η, namely, Eqs. (9) and (10). Since the dependence of the values of ρ, q_p, D_m, and d on c_F can be found experimentally, by comparing Eqs. (9) and (10) it is possible to recover the c_F dependence of η. This will be carried out in Sec. V.

IV. LIGHT SCATTERING DATA

Figure 3 shows the scattered intensity distribution $R(q)$ of five aged gels as a function of the wave vector q. The gels were prepared at different fibrinogen concentrations but under the same physical-chemical conditions of the gelling solution, namely, in TBE at $T = 25 \pm 0.1\,^{\circ}\mathrm{C}$ (see Sec. II). For these gels, the fibrinogen concentration c_F was varied between 0.065–0.611 mg/ml, with the molar ratio thrombin:fibrinogen fixed to 0.01. The data were collected when the gels were already aged, i.e., after a time long enough that their structures have attained a steady-state form, with a consequent stable scattered intensity distribution. All the data appear to be characterized by the same shape of $R(q)$, in which the three different regimes described in the preceding section are clearly present. The figure shows that, though heavier gels scatter much more light than lighter gels, all of them are characterized by fairly similar structures with similar α_m and α_s. The peak position q_p increases with concentration, and this implies that gels prepared at higher c_F exhibit smaller crossover lengths. At the same time the wave vector q_x appears to move toward higher values as gels with smaller c_F are considered, consistently with the picture that lighter gels are formed by thinner fibers. The solid lines are the best fits of the data to Eq. (2).

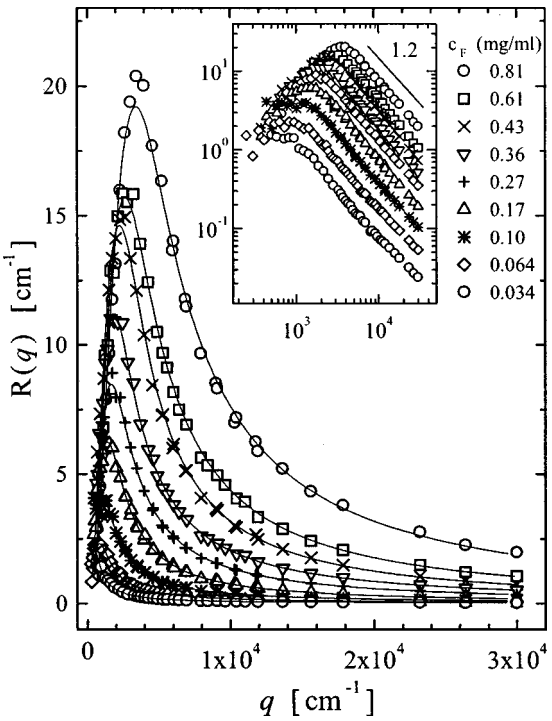

FIG. 4. Low-angle (LAELS) scattered intensity distributions $R(q)$ as a function of the wave vector q for several fibrin gels prepared under the same conditions as those of Fig. 3. Fibrinogen concentration was varied between 0.034–0.81 mg/ml. In the inset, the same data are reported on a log-log scale, and show that all the gels are characterized by the same power-law decay with $\alpha_m \sim 1.2$. For the sake of clarity, not all the measured $R(q)$ have been reported.

As noted previously [9], one of the intriguing features of the data of Fig. 3 is the very small intensity scattered at low wave vectors. As a matter of fact, the data are consistent with a zero-angle asymptotically vanishing scattered intensity, i.e., $R(q=0) \sim 0$. This is fairly evident in Fig. 4, in which the LAELS data corresponding to the five samples of Fig. 3, together with other samples prepared under the same physical-chemical conditions, have been reported on a lin-lin scale. The spanned concentration range, increased with respect to that of Fig. 3, was $c_F = 0.034 - 0.81$ mg/ml. In the inset, the same data are reported on a log-log scale, in which the slope corresponding to $\alpha_m = 1.2$ has been drawn.

A first quantitative analysis of the data of Fig. 4 is reported in Fig. 5, panels A–C, in which various gel parameters for the aged gels are compared and plotted as a function of c_F. Panel A shows that the peak position q_p scales as $q_p \sim c_F^{\beta}$ with $\beta = 0.53 \pm 0.02$. Panel B shows that the intensity scattered at the wave vector $q_f = 10^4$ cm^{-1} belonging to the fractal regime, scales at a fairly high rate, namely, $R(q_f) \sim c_F^{\varphi}$ with $\varphi = 1.41 \pm 0.02$. Lastly, panel C shows that the sample turbidity scales as $\tau \sim c_F^{\mu}$ with $\mu = 1.18 \pm 0.07$.

V. FITTINGS RESULTS

In this section we apply the fitting procedure outlined in Sec. III to analyze the data reported in Sec. IV. The data of

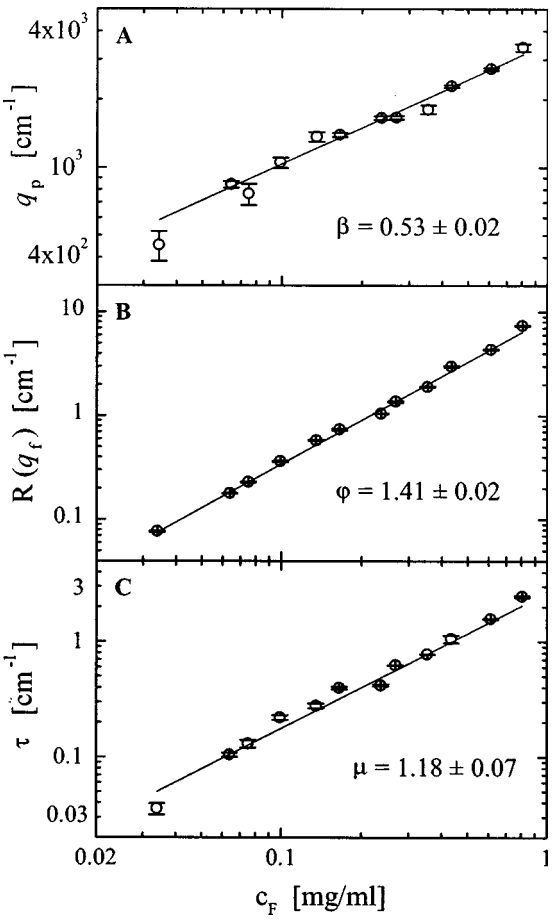

FIG. 5. Behavior of the peak position q_p (Panel A), of the intensity scattered at the wave vector $q_f = 10^4$ cm^{-1} belonging to the fractal regime (Panel B), and of sample turbidity τ (Panel C) as a function of the fibrinogen concentration c_F. The data were derived from the samples of Fig. 4. The straight lines are the best fits of the data to power-law behaviors with respect to c_F, with β, φ, and μ being the corresponding exponents.

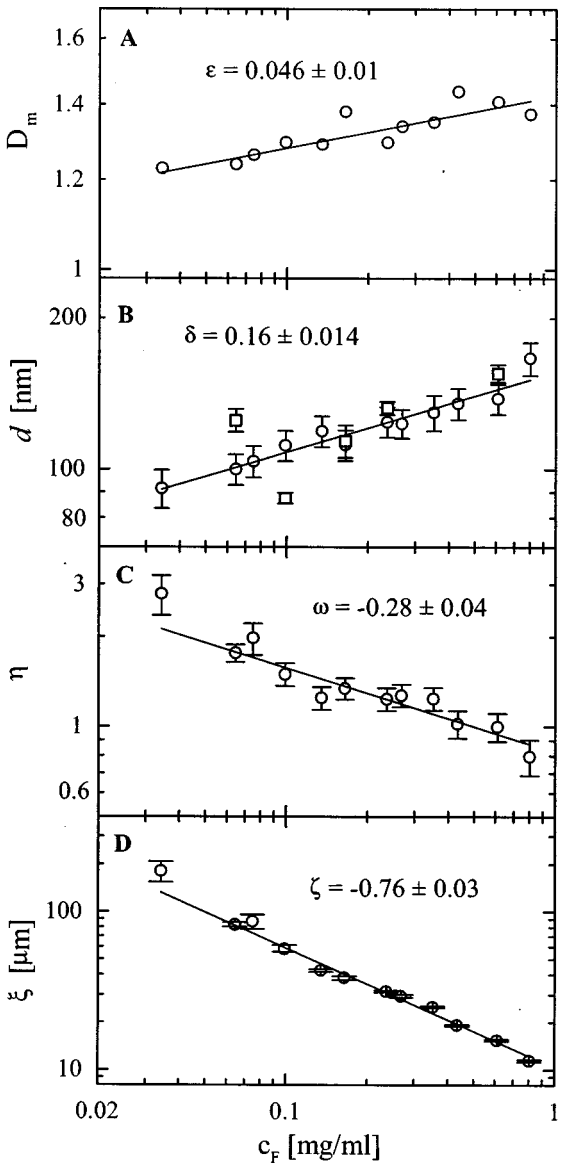

FIG. 6. Behavior of the gel parameters recovered by fitting the LAELS data of Fig. 4 (circles) and the LAELS+CLS data of Fig. 3 (squares) as a function of the fibrinogen concentration c_F. Panel A, mass fractal dimension D_m; Panel B, weight-average fiber diameter d; Panel C, overlapping factor η; Panel D, weight-average gel crossover length ξ. The straight lines are the best fits of the data to power-law behaviors with respect to c_F, with ϵ, δ, ω, and ζ being the corresponding exponents.

Fig. 3 taken over the entire LAELS+CLS q-vector range were fitted to Eq. (2), with the recovered curves shown as solid lines. The fitting was carried out by leaving ρ, ξ, D_m, and d as free parameters, while the remaining ones were fixed to the values $\alpha_s = 4$, $\beta = 1$, $\gamma = 0.28$, and $\ell = 0.4\ \mu$m determined according to the physical considerations reported in Sec. III.

As pointed out above, the recovery of ρ is a direct consequence of measuring $R(q)$ in absolute units. The outputs of our fittings carried out on the data of Fig. 3 show that ρ is similar for all the samples and its average value is $\langle \rho \rangle = 0.4 \pm 0.1$ g/cm^3, in agreement with what we [9] and others [16] have previously reported. Since this value is about 1/3 smaller than the density of the fibrinogen monomers (1.395 g/cm^3), this confirms that inside each fiber the protofibrils are not densely packed, but intertwined with water molecules [9,16].

The value found for ρ was used for fitting the complete set of LAELS data of Fig. 4. Therefore, in this case the free parameters were ξ, D_m, and d, the density was fixed to the value $\rho = 0.4$ g/cm^3, and α_s, β, γ, and ℓ were fixed to the same values as above. The results are reported in Fig. 6, panels A and B, in which the behaviors of D_m and d as functions of c_F are plotted. Figure 6, panel A, shows that the fractal dimension, although confined within the narrow range ~1.2–1.4, exhibit a slight tendency to increase with concentration, suggesting that denser gels are characterized by a somewhat more branched structure. Although the data are consistent with the power-law behavior $D_m \sim c_F^{\varepsilon}$, with $\varepsilon = 0.046 \pm 0.01$, care should be taken not to overinterpret them, given their large spread compared with the spanned range. In any case, their average value is $\langle D_m \rangle = 1.32 \pm 0.07$. Figure 6, panel B, shows that the fiber diameters of

all the gels are also comparable to each other, but in this case there is a clear tendency to have thicker fibers for higher concentration gels. The diameters scale as $d \sim c_F^{\delta}$ with $\delta \sim 0.16 \pm 0.014$. For comparison, the values of the fiber diameters obtained by fitting the full LAELS+CLS data sets of Fig. 3 to Eq. (2) (leaving ρ, ξ, D_m, and d as free parameters) are also reported in Fig. 6, panel B, as open squares. Considering the error bars, the two methods appear to be consistent with each other. It should be also pointed out that the values recovered for D_m and d are independent of the value assigned to the parameter γ (see Appendix B).

At this point, only the c_F dependence of the blob size ξ is still to be found. But first, we have to find out how γ or η depends on concentration. Since we know the dependence of D_m and d on c_F, we can apply the method described in Sec. III and recover the dependence of the overlapping parameter η as a function of c_F. This is shown in Fig. 6, panel C, in which the values of η have been rescaled so that $\eta = 1$ for the concentration $c^* = 0.5$ mg/ml at which the blobs start to overlap. The symbol c^* was adopted by analogy with the same term used by Flory [17] to indicate the overlapping concentration of semidilute polymer solutions (see Sec. VII). The straight line reported on the figure is the best fit of the data to a power-law and shows that η scales as

$$\eta \sim (c_F/c^*)^{\omega},$$

$$\omega \sim -0.28 \pm 0.04, \quad c^* = 0.5 \text{ mg/ml}. \tag{11}$$

The value $c^* = 0.5$ mg/ml was set by fitting the data corresponding to the denser gels. For these samples, the peak is more pronounced and, consequently, the recovery of the parameter γ [or η, via Eq. (8)], is somewhat more reliable. Indeed, if we fit the data corresponding to these gels to Eq. (2) and, besides ρ, ξ, D_m, and d, we leave also γ as a free parameter, the results indicate that η varies around 1 and tends to increase while the concentration decreases. The value $\eta = 1$ occurs for $c_F \sim 0.5$ mg/ml, which falls somewhere in between the second and third higher concentration of the investigated range (0.034–0.81 mg/ml). Equation (11) predicts that, over the entire concentration range, the overlapping factor varies by a factor of ~ 2, from ~ 0.9 at $c_F = 0.81$ mg/ml to ~ 2.1 at $c_F = 0.034$ mg/ml. This means that the denser gels appear to be almost close packed while the lighter gels are expected to be more overlapped. It should be pointed out, however, that for most of the investigated concentrations the recovery of the parameter γ (or η) was not possible, and therefore there was no way to fully test Eq. (11). Nevertheless, at least for the higher concentrations, the recovered values were consistent with Eq. (11), which, consequently, was used for estimating η at all the concentrations.

We can now refit the data of Figs. 3 and 4 to Eq. (2) exactly as done for recovering the parameters D_m and d of Fig. 6, panels A and B, but with the parameter γ fixed to the value obtained by using Eq. (8) with η given by Eq. (11). This allows the recovery of the parameter ξ (the other parameters D_m and d do not change with respect to those obtained with $\gamma = 0.28$, see Appendix B), whose behavior as a function of c_F is shown in Fig. 6, panel D. Differently from the parameter d, for which the scaling exponent is fairly low, ξ scales at a rather higher rate, namely, as $\xi \sim c_F^{\zeta}$ with $\zeta = -0.76 \pm 0.03$. It is worth noticing that the use of the concentration-dependent parameter η is fundamental in order to obtain self-consistent results. Indeed, if we fit the data with $\eta = 1$ (i.e., fixing $\gamma = 0.28$ for all the concentrations), we obtain that ξ scales with c_F differently, with an exponent equal to -0.56 ± 0.07. This would imply that, since $0.56 \sim (3 - \langle D_m \rangle)^{-1}$, with $\langle D_m \rangle = 1.32$, and since $\eta = 1$, the term within square brackets in Eq. (10) should be c_F independent. This is clearly inconsistent with the data (see Fig. 6, panel B).

VI. SCALING

In Sec. V it was shown that all our gels exhibit very similar structures. In this section we investigate how these similarities can be quantitatively characterized and we will verify the self-consistence of the proposed model by using scaling concepts and recasting all the data on a single master curve.

If we replot the data of Fig. 4 in terms of the rescaled wave vector $x = q/q_p$ and rescaled amplitude $R(x) = R(q)/R_p$, being $R_p = R(q_p)$, we obtain the master curve of Fig. 7. This figure shows that all the data tend asymptotically to zero for $x \ll 1$ (better evidenced in the inset), while for $x \gg 1$ they scale as a power-law $R(x) \sim x^{-\alpha_m}$ with $\alpha_m \sim 1.2$. The latter behavior implies a scaling between q_p and R_p. Indeed, since each curve of Fig. 7 decays asymptotically as $R(q) \sim A q^{-\alpha_m}$ with the same α_m but different A, then the master curve can be written (for $x \gg 1$) as

$$R(x) \sim \left[\frac{A(c_F) q_p^{-\alpha_m}}{R_p} \right] x^{-\alpha_m}, \tag{12}$$

in which the dependence of A on c_F has been reported explicitly. Now if Eq. (12) represents a master curve, the term inside the square brackets should be a constant implying that

$$R_p \sim A(c_F) q_p^{-\alpha_m}. \tag{13}$$

Since the amplitude scales as $A(c_F) \sim c_F^{\varphi}$ (see Fig. 5, Panel B), and the peak position as $q_p \sim c_F^{\beta}$ (see Fig. 5, Panel A), it turns out that

$$R_p \sim q_p^{\kappa}, \tag{14a}$$

$$\kappa = -\alpha_m + \frac{\varphi}{\beta}. \tag{14b}$$

By using the values $\alpha_m = 1.2$, $\varphi = 1.41$, $\beta = 0.53$, the expected value for the exponent is $\kappa \sim 1.46$, in fairly good agreement with the value 1.50 ± 0.11 obtained by fitting the data R_p vs q_p with the power-law of Eq. (14a). The scaling behavior between R_p and q_p is illustrated in Fig. 8 on a log-log scale.

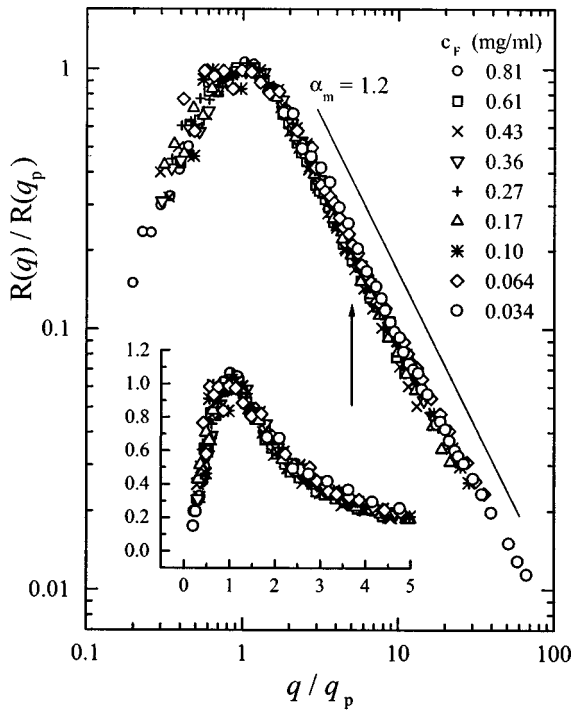

FIG. 7. Scaling behavior of the scattered intensity distributions for the data of Fig. 4 reported in terms of the rescaled amplitude $R(q)/R(q_p)$ versus the rescaled wave vector q/q_p. The existence of a single master curve emphasizes the remarkable similarities between the structure of these gels. The straight line shows the decaying exponent $\alpha_m=1.2$. The inset reports on a lin-lin plot the same data up to $q/q_p=5$ (as indicated by the arrow in the main panel).

One could apply the same reasoning to the $x\ll 1$ region of the master curve and make one more check on the self-consistency of the model. For $x\ll 1$ it results $\gamma\xi q\ll 1$ and Eq. (2) can be approximated to

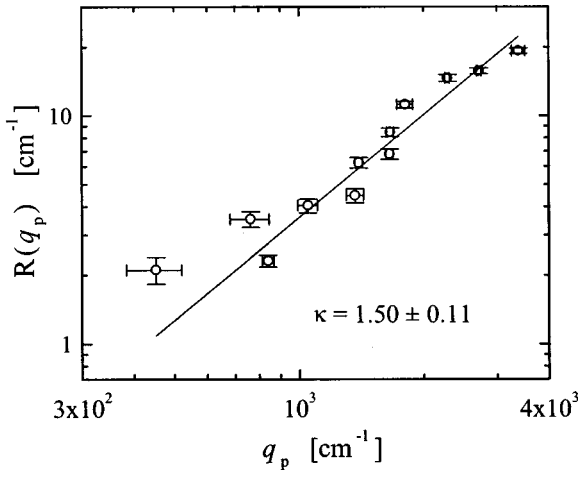

FIG. 8. Behavior of the peak amplitude $R(q_p)$ as a function of the corresponding peak position q_p. The data are taken from the samples of Fig. 4. The exponent $\kappa=1.50\pm0.11$ is consistent with the scaling described in the text.

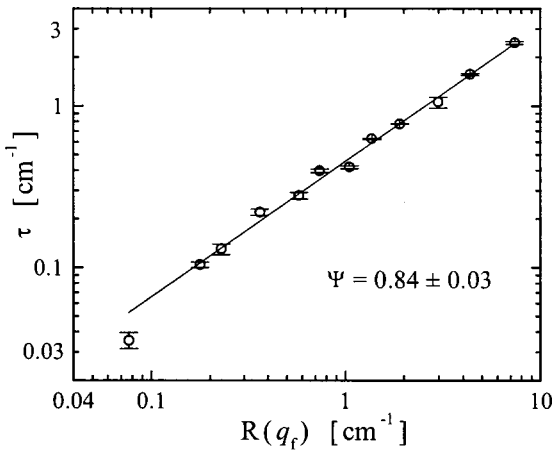

FIG. 9. Scaling behavior of the sample turbidity τ as a function of the intensity $R(q_f)$ scattered at the wave vector $q_f=10^4$ cm^{-1} belonging to the fractal regime. The data are taken from the samples of Fig. 4. The exponent ψ is consistent with the scaling described at the end of Sec. VI and suggests that for length scales smaller than the crossover length ξ all the gels are characterized by the same structure, but with fibers of different size.

$$R(q)\sim Kc_F M\xi^2\gamma^2 q^2, \tag{15}$$

which shows that at very low angles the intensity scales quadratically with q, i.e., $R(q)\sim B(c_F)q^2$, with the amplitude $B(c_F)=Kc_F M\xi^2\gamma^2$. Thus, we can use Eq. (14b) to determine the exponent φ' which characterizes the scaling of B with c_F, i.e., $B(c_F)\sim c_F^{\varphi'}$. By using $\beta=0.53$, $\kappa=1.46$, and setting $\alpha_m'=-2$, it is straightforward to show that $\varphi'=\beta(\kappa-2)\sim-0.29$. Notice that, in principle, this result could have been obtained from the experimental data of Fig. 4, but, unfortunately, in this region the noise level is very high and the wave vector interval over which Eq. (15) holds is rather narrow. Yet, we can use this result for checking the c_F dependence of the overlapping parameter η used in Sec. V. Indeed, from Eq. (15) we can write that $c_F^{\varphi'}\sim c_F M\xi^2\gamma^2$ and recover how γ (or η) scales with c_F, being known the dependencies of M and ξ on c_F. When this calculation is carried out, we find that the scaling exponent for η is -0.32 ± 0.03, consistent with the value of -0.28 ± 0.04 found following the procedure described in Sec. V.

Another way to show the close similarities between the structure of gels at different concentrations is to investigate the dependence of the gel turbidity τ as a function of c_F and compare this behavior (see Fig. 5, Panel C) with the corresponding behavior for the intensity $R(q_f)$ scattered at a wave vector $q_f=10^4$ cm^{-1} belonging to the fractal regime (see Fig. 5, Panel B). If we plot τ against $R(q_f)$, we see in Fig. 9 that the data are nicely described by a power-law behavior $\tau\sim R(q_f)^{\psi}$ characterized by an exponent $\psi=0.84\pm0.03$. This means that the turbidity increases with c_F at a slower rate than the scattered intensity. In our previous work [9] we showed that, after the initial scaffold is formed, the gel growth consists mainly of a thickening of the fibers without any substantial change in its structure. Thus, when the fibers grow so thick that they become comparable with the wave-

length of light, the turbidity τ scales with $R(q_f)$ as a power-law characterized by an exponent ψ, which depends only on D_m, namely, $\psi=(2+D_m)/4$. Now, the data of Fig. 9 exhibit exactly this behavior. Moreover, if we use for D_m its average value $\langle D_m\rangle=1.32\pm0.07$, we find that also the exponent is in excellent agreement with the expected value, $\psi=0.83\pm0.02$. Thus, except for their crossover length ξ, gels at different concentrations appear to be characterized by the same inner structure, but with fibers of different size.

VII. SUMMARY AND DISCUSSION

In this work we have studied the dependence of the structure of fibrin gels on the concentration of the fibrinogen monomers. The gels were formed under quasiphysiological conditions, and the reaction was initiated by monomer activation via the enzyme thrombin at a constant molar ratio. The intensity distributions scattered from the gels were measured in absolute units over a very wide range of scattering wave vectors (up to about three decades), and were interpreted in terms of a simple structural model recently proposed by us [9] and futher developed here. The model describes the gel as a random network of fibers of density ρ and average diameter d entangled together to form densely packed and spatially correlated blobs of mass fractal dimension D_m and average size ξ, which overlap by a factor η. Although the model was originally developed for a monodisperse system, we have shown that it is still valid when the gel is made of blobs of different size and assembled with fibers of different thickness. The issue of polydispersity in the fiber diameter d was addressed in Ref. [9], in which it was shown that the diameter d recovered by fitting the data with Eq. (2) is actually a root-mean-square weight-average diameter, i.e., $d\sim\sqrt{\langle d^2\rangle_w}$. In this work, we extended this analysis and demonstrated that also ξ is a reasonable estimate of the weight-average blob size $\langle\xi\rangle_w$, i.e., $\xi\sim\langle\xi\rangle_w$.

By varying the fibrinogen concentration c_F between 0.034–0.81 mg/ml we have obtained gels whose parameters scale as power laws with c_F and vary over the following ranges: $100\geqslant\xi\geqslant10$ μm, $100\leqslant d\leqslant200$ nm, $1.2\leqslant D_m\leqslant1.4$, $2\geqslant\eta\geqslant1$, and constant $\rho\sim0.4$ mg/ml. An important finding of this work is that, in order to ensure the self-consistency between the data and the model, the blobs must partially overlap by a factor $\eta=\xi/\xi_0$, ξ_0 being the average distance between the blobs. Thus, provided that η is allowed to vary with c_F, all the gel parameters reported above scale with c_F according to the model. It must be pointed out that the overlapping affects relevantly the relation between the crossover length (or average blob size) ξ and the effective gel mesh size, i.e., the average distance between the fibers in the gel. In Ref. [9] we suggested that, since D_m is close to unity ($D_m\sim1.3$), the blobs can be thought of as an assembly of a few semirigid fibers grown by joining together many segments with only a few branching points. It follows that the average distance between the fibers inside the blob is not much smaller than the size of the blob itself. Thus, if $\eta=1$, the blobs are in contact with each other, and the blob size ξ provides at least an upper bound of the overall average distance between the fibers in the whole gel. Clearly, this reasoning fails when the blobs overlap and $\eta>1$. In this case the fibers belonging to one blob interpenetrate with fibers of other blobs and, consequently, the overall gel mesh size decreases, becoming smaller than the average blob size. Thus, we expect that the gel mesh size depends on both the blob size ξ and the overlapping parameter η. It is, however, beyond the purpose of this paper to tackle the problem of providing an estimate of the gel mesh size from our scattering data, and we defer this complex issue to a future work.

In any case, comparing our findings with the available literature data it is not an easy task, because of the different conditions under which the gels were formed. For instance, Blombäck *et al.* [18] have examined by confocal laser microscopy, turbidity and permeability, the characteristics of fibrin gels formed at various fibrinogen concentrations, but at constant thrombin concentration (0.35 NIH units/ml), in a buffer otherwise identical to ours were not for the presence of 20 mM $CaCl_2$. In addition, the fibrinogen concentrations investigated by Blombäck *et al.* [18] covered a higher range in respect to ours (0.5–4.0 vs 0.03–0.8 mg/ml, respectively), with just a small overlap region. These rather profound differences notwithstanding, it is interesting to note that the fiber diameters deduced from their turbidity data (Table 1A of Ref. [18]) increase with increasing the fibrinogen concentration, as in our case. However, the same authors also deduced fiber diameters from their permeability data (Table 1A of Ref. [18]), and in this case no concentration dependence was found. It is possible that this is an effect due to the polydispersity of fiber diameters, which affects the two techniques differently, as already suggested [19]. An increase in fiber diameter with increasing fibrinogen concentration at constant thrombin concentration was also predicted by Weisel and Nagaswami [20] from computer models of fibrin polymerization kinetics based on turbidimetry and electron microscopy observations, although no quantitative estimates were provided. Finally, Ryan *et al.* [21] found an opposite, weak trend by analyzing computerized three-dimensional models constructed from stereo pairs of scanning electron micrographs of fibrin gels grown, at constant thrombin concentration (1 NIH units/ml), in solution conditions almost identical to ours but in absence of EDTA-Na_2 (see Tables 1 and 2 and Fig. 3A of Ref. [21]). Thus, as already pointed out by Ryan *et al.* [21], this issue is still controversial, and it is unfortunate that no other data are available, to the best of our knowledge, on the concentration dependence of the properties of fibrin gels prepared at constant molar ratio with the activating enzyme. Clearly, more experimental data are needed to better assess this issue.

Returning to our data, Table I summarizes the scaling behavior that we found for ρ, d, D_m, ξ, η, and other gel parameters by reporting the scaling exponent, the prefactor and the range spanned by each parameter. The prefactor indicates the parameter value in correspondence of the concentration $c^*=0.5$ mg/ml, as was done in Eq. (11). Synthetically, for a generic parameter x, $x(c_F)=A_x(c_F/c^*)^z$, where z is the exponent associated with x and A_x the corresponding prefactor. Thus, expressing also c_F in mg/ml, it is possible to predict the value of any of the measured parameters at any particular concentration c_F.

TABLE I. Scaling behaviors of the various parameters characterizing fibrin gels as a function of the fibrinogen concentration c_F (0.034–0.81 mg/ml). The prefactors have been normalized to the concentration $c^*=0.5$ mg/ml. For each parameter x the value at c_F can be found according to $x(c_F)=A_x(c_F/c^*)^z$, where z is the exponent associated with x and A_x the corresponding prefactor.

Parameter	Exponent	Exponent value	Prefactor	Spanned range
q_p (cm^{-1})	β	0.53 ± 0.02	2444 ± 37	581–3162
$R(q_f)$ (cm^{-1})	φ	1.41 ± 0.02	3.29 ± 0.11	0.075–6.49
τ (cm^{-1})	μ	1.18 ± 0.07	1.17 ± 0.03	0.0033–2.07
ρ (g/cm^3)			0.4 ± 0.1	0.4 (constant)
d (nm)	δ	0.16 ± 0.014	140 ± 2.5	91.0–151.2
D_m	ε	0.046 ± 0.01	1.38 ± 0.02	1.22–1.41
ξ (μm)	ζ	-0.76 ± 0.03	17.5 ± 0.4	133–12.2
η	ω	-0.28 ± 0.04	1.00 ± 0.05	2.1–0.9

Although it would be unwise to use the relations of Table I for extrapolating the value of the parameters at concentrations much higher than the highest investigated in the present study, ~0.8 mg/ml, we could reasonably expect that they may hold up to the physiological range, ~3 mg/ml. At these concentrations, it would be rather difficult to perform light scattering experiments such as those reported here, due to the increase in turbidity and multiple scattering problems. Shorter pathlength cells could be used, but this in turn will bring mixing problems and capillarity effects. For instance, for $c_F=3$ mg/ml we estimate $d\sim186$ nm and $\xi\sim4.5$ μm, with $\eta\sim0.6$ and $D_m\sim1.5$. Due to the differences in solution conditions stated above, we can only attempt a comparison of the estimated diameter value with those reported by Ryan *et al.* [21] for $c_F=3$ mg/ml (see Tables 1 and 2 and Fig. 3B of Ref. [21]). For this c_F, our thrombin concentration at a 1:100 molar ratio with fibrinogen should be $\sim3.26\times10^{-3}$ mg/ml, implying that ~6.5 NIH units/ml would be present according to the stated activity of ~2000 NIH units/mg of protein. A later estimate of the NIH units content of this batch of thrombin, carried out by us by comparing its clotting efficiency with a newer batch, suggested that roughly half of the original activity was still present (~1150 NIH units/mg protein), leading to a value of ~3.75 NIH units/ml at $c_F=3$ mg/ml. Thus, it is reasonable to compare our predicted data with those of ''clot E'' reported in Table 2 of Ryan *et al.* [21], which was obtained at 5 NIH units/ml. Recalling that our hydrated diameters should be roughly 1.8 times bigger than the unhydrated diameters seen in the electron microscope [9], and that the polydispersity index of similar samples is $\langle d^2\rangle_w/\langle d^2\rangle_n\sim1.23$ (see Appendix A), we can compute a number-average unhydrated diameter of ~93 nm. While this number is within the observed range of values (20–130 nm) reported by Ryan *et al.* [21], it is about twice their number average diameter (44 ± 15 nm). Considering the roughness of these computations, we think that our predicted d value measures up reasonably well with the available electron microscope evidence.

Finally, it is interesting to compare our findings with the results known from the physics of semidilute solutions of polymeric linear chains [17,22]. In this case, the equivalent of the close packing condition for the blob model [Eq. (10)] is expressed in terms of the so-called overlapping concentration c^*. Following the classical theory of Flory [17], c^* represents the concentration at which the chains *start* to overlap, and is related to the chain size R_F by $R_F\sim(c^*)^{-\nu/(3\nu-1)}$. Here, ν is the Flory exponent that describes the scaling $R_F\sim\ell n^\nu$ between the chain size, the chain segment ℓ, and the number n of segments per chain. As is known, ν depends on the segment-segment and segment-solvent interactions, and can vary between 1/3 (globular coils) and 1 (rigid rods), passing through the well known values of $\nu=0.5$ (random coils) and $\nu=0.6$ (coils with excluded volume interactions). When $c\gg c^*$, the chains strongly interact, and the solution can gel via the formation of crosslinks between the different chains. Under these conditions, the characteristic length scale of the system is no longer R_F, but the average distance between the crosslinks that corresponds to the gel mesh size ξ and is customarily called correlation length of the gel [22]. Since each chain can make several crosslinks, we expect that $\xi<R_F$. de Gennes suggested [22] that the portion of the chain between two crosslinks could be imagined as a blob and that inside each blob the interactions would be dominated by the monomer-monomer interaction of a single chain. Under this picture, although the chains overlap with each other, the blobs do not, and they are close packed with ξ scaling with c as R_F scales with c^*. As a result, based on scaling concepts, the Flory–de Gennes theory of gels predicts that for a gel in good solvent the mesh size behaves as $\xi/R_F\sim(c/c^*)^{-\nu/(3\nu-1)}$, a relation that was verified experimentally by a number of different research groups (see Ref. [23] and references therein).

Thus, the picture of the Flory–de Gennes gels and our blob model appear to be equivalent provided that $\nu=1/D_m$, but only if we neglect the overlapping between our blobs and set $\eta\sim1$. In this case the mesh size of the Flory–de Gennes theory would correspond to the blobs' average size or crossover length ξ of our gels. If we derive a value for ν from our D_m values (~1.2–1.4), we find $0.71\leqslant\nu\leqslant0.83$, which would indicate that the blobs are made of polymers having intermediate properties between those of random coils and rods. This is quite consistent with the picture that emerged from our previous studies on the early stages of fibrin polymerization [7,24] when we found that the protofibrils can be best described as double-stranded, half-

staggered, wormlike chains with persistence lengths between 200–600 nm. Moreover, in our recent work on the structure of fibrin gels [9], we also showed that, in alternative to the blob model, the data could be interpreted as deriving from a collection of wormlike chains polydisperse in width and persistence length. By using the Flory–de Gennes theory with the values derived above for ν, one would find that ξ scales with c as $\xi \sim c^{\zeta}$ with $-0.63 \leqslant \zeta \leqslant -0.56$, which is less than what we observed experimentally, namely, $\zeta = -0.76 \pm 0.03$ (see Table I). One may notice that the exponent -0.56 is remarkably close to the value that one would obtain by simply estimating ξ as the reciprocal of the peak position in $R(q)$, that is, $\xi \sim q_p^{-1} \sim c_F^{-0.53}$ (see Table I). However, this would imply that there is no overlapping, which makes the model inconsistent with the data. One may also notice that, if we estimate a value for ν from the ζ exponent, we obtain $\nu \sim 0.6$, which is exactly what was expected for coils with excluded volume interactions. We believe that this is only a coincidence, inconsistent with our D_m values ($D_m = 1/\nu$), and we warn the reader not to be brought to the conclusion that the blobs of our model behave as linear coils in a good solvent with excluded volume interactions. The two systems appear to be very much different: first of all, the Flory–de Gennes theory deals with linear polymers obtained by assembling monodisperse segments (same length ℓ, same diameter d), while our fibers appear to be characterized by similar ℓ, but are polydisperse in d. Second, our blobs appear to be made of somewhat semiflexible branched fibers (see, for example, the pictures of Fig. 2 in Ref. [21]) whose diameters grow in the course of gelation and vary with c_F as well. Thus, part of available mass goes into fiber thickening, and is not used for the rescaling of ξ.

In conclusion, notwithstanding the remarkable and intriguing similarities between our blob model and the Flory–de Gennes theory, we believe that the two descriptions do not fully fit each other. Probably, by reshaping our blob model in terms of a dense collection of wormlike chains highly polydisperse in their persistence length, we would make the system more suitable for being described in the framework of the Flory–de Gennes theory, and provide a better understanding of the overall gel structure. Clearly, more experimental data taken under different physical-chemical conditions of the gelling solution, and while the samples are gelling, would be very helpful. We are currently working in that direction.

ACKNOWLEDGMENTS

We thank Enrico Di Cera for his generous gift of titrated hirudin, Raimondo De Cristofaro for his help in determining the thrombin concentration, Davide Magatti for his contribution to data analysis, and Aldo Profumo and Marco Turci for performing fibrinogen analyses and clotting assays. This work was supported by grants from Consiglio Nazionale delle Ricerche (CNR) to G.A. and F.F., Istituto Nazionale Fisica della Materia (INFM) to M.G., and Agenzia Spaziale Italiana (ASI) to M.R. and F.F.

APPENDIX A

In this appendix we address the issue of how the presence of polydispersity in both ξ and d affects the structural model proposed for the gel. In particular, we show how Eqs. (9) and (10) are modified by polydispersity and, correspondingly, what kind of average value for ξ can be recovered from the data.

We start with Eq. (9) by recalling that the expressions given in Sec. III for the scattered intensity distribution [Eqs. (1) and (2)] are valid for a monodisperse system, i.e., a gel in which all the blobs have the same size ξ and same fiber diameter d. The presence of polydispersity transforms Eq. (2) into [12]

$$R(q) = K\, c_F \langle M \rangle_w\, S^{\mathrm{eff}}(q) \langle P(q) \rangle_z , \tag{A1}$$

where $\langle M \rangle_w$ is the weight-average molecular weight of the blobs, $\langle P(q) \rangle_z$ is their z-average form factor [$\langle P(q) \rangle_z = \langle A(q) B(q) \rangle_z$], and $S^{\mathrm{eff}}(q)$ represents the effective structure factor that describes the effects of spatial correlations between the polydisperse blobs.

$S^{\mathrm{eff}}(q)$ can be easily found from the corresponding expression for the monodisperse case, $S(q)$. The latter one was based on the relation $\xi_0^3 \sim \langle N/V \rangle$, which describes how the distance ξ_0 between the close packed monodisperse blobs scales with the number density N/V. For a polydisperse system such a relation becomes $\langle \xi_0^3 \rangle_n \sim \langle N/V \rangle$ where $\langle \cdots \rangle_n$ means number-average. Now, since $\xi \sim \eta \xi_0$, it is clear that the parameter ξ appearing in $S(q)$ has to be replaced with $\langle \xi^3 \rangle_n^{1/3}$. Thus, the effective structure factor becomes

$$S^{\mathrm{eff}}(q) = 1 - \beta e^{-(\gamma \langle \xi^3 \rangle_n^{1/3} q)^2} \tag{A2}$$

and the asymptotic behavior at low q ($\gamma \langle \xi^3 \rangle_n^{1/3} q \ll 1$) of the scattered intensity distribution is

$$R(q) = K c_F \langle M \rangle_w \gamma^2 \langle \xi^3 \rangle_n^{2/3} q^2 , \tag{A3}$$

in which we have used $\beta = 1$ as suggested by the data. Eq. (A3) is represented graphically in Fig. 2 by the leftmost solid straight line passing through the data.

The expression for $\langle P(q) \rangle_z$ was already developed in Ref. [9]. Here we will report only the results relative to its approximation in the fractal regime ($\xi^{-1} \ll q \ll \ell^{-1}$, d^{-1}), in which the scattered intensity distribution becomes

$$R(q) = K c_F \langle M \rangle_w \pi^{D_m} \langle \xi^{-D_m} \rangle_z\, q^{-D_m} \tag{A4}$$

or equivalently, via Eq. (1),

$$R(q) = \frac{\pi^{1+D_m}}{4} K c_F N_A\, \rho \langle \ell^{l-D_m} d^2 \rangle_w\, q^{-D_m} . \tag{A5}$$

Equations (A4) and (A5) are the generalization to polydispersity of Eqs. (4) and (5), respectively. Equation (A5) shows that the diameter d recovered by fitting the data with Eq. (2) is actually a root-mean-square weight-average diameter, i.e., $d \sim \sqrt{\langle d^2 \rangle_w}$. The behavior described by Eq. (A4) or (A5) is represented graphically by the central solid straight line of Fig. 2.

An estimate of the peak position q_p can be carried out as done for Eq. (3), i.e., by finding the wave vector at which the two asymptotic behaviors for $q \to 0$ and q belonging to the fractal regime cross to each other. Thus by equating Eqs. (A3) and (A4), it is straightforward to work out that, if we define the x-average of ξ as

$$\langle \xi \rangle_x = \left[\frac{\langle \xi^3 \rangle_n^{2/3}}{\langle \xi^{-D_m} \rangle_z} \right]^{1/(2+D_m)}, \tag{A6}$$

the generalization of Eq. (3) becomes

$$\langle \xi \rangle_x \sim 1.3 \pi^{2/(2+D_m)} \gamma^{-2/(2+D_m)} (q_p)^{-1}, \tag{A7}$$

in which we have introduced the same numerical factor of 1.3 as in Eq. (3). It is worth noticing that $\langle \xi \rangle_x$ is a combination of a number-average and a z-average. Therefore, because the blob mass is a function of both ξ and d [see Eq. (1)] $\langle \xi \rangle_x$ depends on the joint distribution which characterizes the polydispersity of both ξ and d. However, if we make the plausible assumption that ξ and d are statistically independent variables, the dependence on d disappears, and $\langle \xi \rangle_x$ becomes only a function of the polydispersity in ξ, and can be written as

$$\langle \xi \rangle_x = \left[\frac{\langle \xi^3 \rangle_n^{2/3} \langle \xi^{2D_m} \rangle_n}{\langle \xi^{D_m} \rangle_n} \right]^{1/(2+D_m)}. \tag{A8}$$

It is now easy to compare $\langle \xi \rangle_x$ with the more common averages and $\langle \xi \rangle_n$, $\langle \xi \rangle_w$, and $\langle \xi \rangle_z$. A simple numerical analysis carried out with $D_m = 1.3$ shows that, for bell shaped distributions, $\langle \xi \rangle_x$ depends only on the relative width $\sigma_n / \langle \xi \rangle_n$ and it is very well approximated by $\langle \xi \rangle_w$ with deviations of less than -4% ($\langle \xi \rangle_x / \langle \xi \rangle_w \geqslant 0.96$) up to $\sigma_n / \langle \xi \rangle_n \sim 50\%$. Conversely, with respect to $\langle \xi \rangle_n$ and $\langle \xi \rangle_z$ the deviations are much higher, of the order of $+25\%$ and -20%, respectively. For more skewed distribution, such as decaying power laws or exponentials, the matching of $\langle \xi \rangle_x$ with $\langle \xi \rangle_w$ is less accurate, but still much better than with $\langle \xi \rangle_n$ or $\langle \xi \rangle_z$. For example, for an exponential decay (for which $\sigma_n / \langle \xi \rangle_n = 1$) the deviation is $\sim -11\%$. So in conclusion, we can state that the value of $\langle \xi \rangle_x$ obtained by means of the peak position q_p is a reasonable estimate of the weight-average blob size $\langle \xi \rangle_w$ of the gel.

We come now to discuss Eq. (10). This was worked out by equating the gel concentration c_F to the ratio between the blob mass M/N_A given by Eq. (1) and the blob volume ξ_0^3. When there is polydispersity this relation becomes

$$c_F \sim \frac{\langle M/N_A \rangle_n}{\langle \xi^3 / \eta^3 \rangle_n} = \rho \frac{\pi}{4} \eta^3 \langle \ell^{1-D_m} d^2 \rangle_n \frac{1}{\langle \xi^{3-D_m} \rangle_w}, \tag{A9}$$

in which we have again assumed that ξ and d are statistically independent and used Eq. (1) together with the relation $\langle \xi^{D_m} \rangle_n / \langle \xi^3 \rangle_n = 1 / \langle \xi^{3-D_m} \rangle_w$. Thus, by defining the y-average of ξ as

$$\langle \xi \rangle_y = [\langle \xi^{3-D_m} \rangle_w]^{1/(3-D_m)}, \tag{A10}$$

Eq. (A9) can be rewritten as

$$\langle \xi \rangle_y \sim c_F^{-1/(3-D_m)} \eta^{3/(3-D_m)} \left(\frac{\pi}{4} \rho \langle \ell^{1-D_m} d^2 \rangle_n \right)^{1/(3-D_m)}, \tag{A11}$$

which generalizes Eq. (10). As done above, we can compute numerically how $\langle \xi \rangle_y$ compares with $\langle \xi \rangle_n$, $\langle \xi \rangle_w$, and $\langle \xi \rangle_z$. The results are very similar to those obtained for $\langle \xi \rangle_x$ and show that, for bell shaped distributions with up to $\sigma_n / \langle \xi \rangle_n \sim 50\%$, the deviations from $\langle \xi \rangle_w$ are less than approximately $+5\%$. For more skewed distributions the situation is similar to that of $\langle \xi \rangle_x$. So, we can state that also the parameter $\langle \xi \rangle_y$, which describes the condition of close packing, is reasonably approximated by $\langle \xi \rangle_w$. It should be noticed that in Eq. (A11) the average diameter d appears as the number-average cross section $\langle d^2 \rangle_n$, thus not directly comparable with the value recovered from the data via Eq. (5), which depends on $\langle d^2 \rangle_w$.

In conclusion, when polydispersity effects on ξ are taken into account, the value obtained for ξ from the peak position and the one used for verifying the close packing condition of the model, are both to be interpreted as good estimates of the weight-average blob size $\langle \xi \rangle_w$. In this way, the self-consistency of the model is preserved.

When polydispersity effects on d are considered, the situation is more complicated because from the data we can recover only $\langle d^2 \rangle_w$, while in the close packing condition appears $\langle d^2 \rangle_n$. Thus the self-consistency is maintained only if the polydispersity in d is comparable for all the gels, and if we can suppose that the ratio $\langle d^2 \rangle_w / \langle d^2 \rangle_n$ remains the same for all the concentrations. Unfortunately, to our knowledge there are no data available in the literature on this subject. The only published work [25] in which are reported the electron microscopy-derived actual histograms of the fiber diameter distributions of a gel grown under physical-chemical conditions similar to ours (but in the presence of 2 mM $CaCl_2$), deals with a single concentration [see Fig. 4, panel (c) of Ref. [25]]. In that case ($c_F = 0.5$ mg/ml) the polydispersity in diameter was moderately broad, with $\sigma_n / \langle d \rangle_n \sim 0.25$ and $\langle d^2 \rangle_w / \langle d^2 \rangle_n \sim 1.23$. This implies an overestimate of $\langle \xi \rangle_y$ by only a factor of $\sim 13\%$ (for $D_m = 1.3$) and, therefore, we believe that even a non-negligible dependence of the ratio $\langle d^2 \rangle_w / \langle d^2 \rangle_n$ on c_F should not alter significantly the behavior of $\langle \xi \rangle_y$ predicted by the model.

APPENDIX B

In this appendix we recall the method recently developed by us [9] for the recovery of the diameter d, and propose a variant that leads to much more accurate results.

We demonstrated [9] that, even without having access to the crossover wave vector q_x [see Eq. (6)], one can exploit the fact that the scattered intensity is measured in absolute units and recover d by using the LAELS data alone. Indeed, provided that the gel parameters ρ and ℓ are known [or recoverable by fitting the data over the entire LAELS+CLS wave vector range to Eq. (2)], one can fit the straight portion of the data between q_p and q_x to Eq. (5) and extract the values of both D_m and d. However, this procedure is not extremely accurate and leads to some systematic errors in the

estimate of both D_m and d. This is because the condition that defines the right-hand side of the fractal regime ($q \ll \ell^{-1}, d^{-1}$) is not fulfilled with high accuracy over the entire wave vector range where the LAELS data appear to be straight. Thus, the contribution of the baseline $(\ell/\xi)^{D_m}$ appearing in the term $A(q)$ of the fitting function [Eq. (2)] is not completely negligible with respect to the power-law contribution $(\pi/q\xi)^{D_m}$, and the term $B(q)$ is also less than 1. For example, if $\ell = 0.4\ \mu$m, and $d = 150$ nm, at the maximum wave vector of the LAELS measurements ($\sim 3 \times 10^4$ cm^{-1}), the term $A(q)$ deviates from the power-law behavior by a $\sim +30\%$ contribution, while the term $B(q)$ is lower than 1 by approximately $\sim -7\%$. Though these two deviations tend to balance each other, the first one is predominant and produces a slight upward rounding of the power-law decay, leading to an underestimation of D_m and, in turn, to an overestimation of d. This was tested by computer simulations in which synthetic data generated according to Eq. (2) (with $\rho = 0.4$ g/cm^3, $\xi = 20\ \mu$m, $D_m = 1.3$, $d = 150$ nm, $\ell = 0.4\ \mu$m, $\alpha_s = 4$, $\beta = 1$, and $\gamma = 0.28$) were fitted in the fractal regime by means of Eq. (5). The wave vector range of the selected data was chosen between $\sim 5 \times 10^3 - 3 \times 10^4$ cm^{-1}, so as to closely match the range used in the experimental data of Fig. 4. By supposing to know the parameters ρ and ℓ, the fitting recovered d with an error of $\sim +15\%$, while D_m was underestimated by a factor of $\sim -10\%$, which corresponds to the exponent $\alpha_m \sim 1.2$ of Fig. 2.

In this paper we propose a slightly different procedure of fitting the LAELS data. If, instead of the tract in which the data exhibit a power-law decay, all the LAELS data (including the peak) are used and fitted to the entire model function [Eq. (2)], much better accuracies can be achieved for both D_m and d. Computer simulations (carried out on the same synthetic data as above) showed that, by leaving ξ, D_m, and d as free parameters, fixing all the others to the correct values, and including the data between $\sim 1 \times 10^3 - 3 \times 10^4$ cm^{-1}, the values of D_m and d can be both estimated with accuracies better than 1%. We also checked that the accurate recovery of D_m and d is independent from the value assigned to the parameter γ. In other words, even if the fitting is carried out by fixing γ to a wrong value (for example, up to a factor ~ 2), D_m and d are recovered always with the same level of accuracy, consistently with the fact that, in the fractal regime, the scattering amplitude does not depend on the spatial arrangement of the blobs, i.e., it does not depend on γ. Finally, we would like to emphasize that this procedure works because, up to wave vectors of $\sim 3 \times 10^4$ cm^{-1}, the shape of $R(q)$ is only slightly dependent on d, while its amplitude scales as d^2 [through the term M appearing in the prefactor of Eq. (2)].

[1] R. F. Doolittle, Annu. Rev. Biochem. **53**, 195 (1984).
[2] B. Blombäck, Thromb. Res. **83**, 1 (1996).
[3] C. M. Jackson and Y. Nemerson, Annu. Rev. Biochem. **49**, 765 (1980); V. Costantini and L. R. Zacharski, Thromb. Haemostasis **69**, 406 (1993).
[4] D. L. Stocum, Wound Repair Regen **6**, 276 (1998); A. Haisch, A. Loch, J. David, A. Pruss, R. Hansen, and M. Sittinger, Med. Biol. Eng. Comput. **38**, 686 (2000).
[5] J. H. Brown, N. Volkmann, G. Jun, A. H. Henshen-Edman, and C. Cohen, Proc. Natl. Acad. Sci. U.S.A. **97**, 85 (2000); Z. Yang, J. M. Kollman, L. Pandi, and R. F. Doolittle, Biochemistry **40**, 12515 (2001).
[6] Z. Yang, I. Mochalkin, and R. F. Doolittle, Proc. Natl. Acad. Sci. U.S.A. **97**, 14156 (2000).
[7] S. Bernocco, F. Ferri, A. Profumo, C. Cuniberti, and M. Rocco, Biophys. J. **79**, 561 (2000).
[8] E. Di Stasio, C. Nagaswami, J. W. Weisel, and E. Di Cera, Biophys. J. **75**, 1973 (1998).
[9] F. Ferri, M. Greco, G. Arcòvito, M. De Spirito, E. Paganini, and M. Rocco, Phys. Rev. E **63**, 031401 (2001). Note: due to a typing error, a wrong value of the optical constant K was reported in this reference. The correct value is $K = 2.68 \times 10^{-7}$ cm^2/g^2.
[10] D. Q. Dang and E. Di Cera, J. Protein Chem. **13**, 367 (1994).
[11] M. De Spirito, G. Arcòvito, F. Andreasi-Bassi, M. Rocco, E. Paganini, M. Greco, and F. Ferri, Nuovo Cimento Soc. Ital. Fis., D **20D**, 2409 (1998).
[12] M. Kerker, *The Scattering of Light and Other Electromagnetic Radiation* (Academic, New York, 1969).
[13] G. Dietler, C. Aubert, D. S. Cannell, and P. Wiltzius, Phys. Rev. Lett. **57**, 3117 (1986); **59**, 246 (1987).
[14] M. Carpineti and M. Giglio, Phys. Rev. Lett. **68**, 3327 (1992).
[15] R. Vacher, T. Woignier, J. Pelous, and E. Courtens, Phys. Rev. B **37**, 6500 (1998).
[16] M. E. Carr, Jr. and J. Hermans, Macromolecules **11**, 46 (1978).
[17] P. Flory, *Principles of Polymer Chemistry* (Cornell University Press, Ithaca, NY, 1969).
[18] B. Blombäck, K. Carlsson, B. Hessel, A. Liljeborg, R. Procyk, and N. Åslund, Biochim. Biophys. Acta **997**, 96 (1989).
[19] G. A. Shah, I. A. Ferguson, T. Z. Dhall, and D. P. Dhall, Biopolymers **21**, 1037 (1982).
[20] J. W. Weisel and C. Nagaswami, Biophys. J. **63**, 111 (1992).
[21] E. A. Ryan, L. F. Mockros, J. W. Weisel, and L. Lorand, Biophys. J. **77**, 2813 (1999).
[22] P. G. de Gennes, *Scaling Concepts in Polymer Physics* (Cornell University Press, London, 1979).
[23] W. Brown and T. Nicolai, Colloid Polym. Sci. **268**, 977 (1990).
[24] M. Rocco, S. Bernocco, M. Turci, A. Profumo, C. Cuniberti, and F. Ferri, Ann. N.Y. Acad. Sci. **936**, 167 (2001).
[25] T. C. Baradet, J. C. Haselgrove, and J. W. Weisel, Biophys. J. **68**, 1551 (1995).